Applied Surface Science 257 (2011) 8038–8043

Applied Surface Science

journal homepage: www.elsevier.com/locate/apsusc

Analyses of residual iron in carbon nanotubes produced by camphor/ferrocene pyrolysis and purified by high temperature annealing

E.F. Antunes[a,b,*], V.G. de Resende[b], U.A. Mengui[b], J.B.M. Cunha[c], E.J. Corat[b], M. Massi[b]

[a] Instituto Tecnológico de Aeronáutica (ITA), Praça Marechal Eduardo Gomes, 50, CEP 12.228-900, São José dos Campos, SP, Brazil
[b] Instituto Nacional de Pesquisas Espaciais (INPE), Av. dos Astronautas, 1758, CEP 12.227-010, São José dos Campos, SP, Brazil
[c] Universidade Federal do Rio Grande do Sul (UFRGS), Av. Bento Gonçalves, 9500, CEP 91.501-970, Porto Alegre, RS, Brazil

ARTICLE INFO

Article history:
Received 7 April 2011
Received in revised form 20 April 2011
Accepted 21 April 2011
Available online 27 April 2011

Keywords:
Carbon nanotubes
Purification
Annealing
Mossbauer spectrocopy
Camphor
XPS

ABSTRACT

A detailed analysis of iron-containing phases in multiwall carbon nanotube (MWCNT) powder was carried out. The MWCNTs were produced by camphor/ferrocene and purified by high temperature annealing in an oxygen-free atmosphere (N_2 or VC). Thermogravimetric analysis, Mössbauer spectroscopy, X-ray diffraction and X-ray photoelectron spectroscopy enabled the evaluation of the residual iron in MWCNTs after purification. The VC treatments provided MWCNTs with a purity degree higher than 99%. Moreover, Raman spectroscopy revealed a significant improvement in graphitic ordering after thermal annealing. A brief description of the mechanism of iron removal was included. We highlight the mobility of iron atoms through graphitic sheets and the large contact angle of iron clusters formed on MWCNT surfaces at high temperatures.

1. Introduction

High temperature annealing in nonoxidative atmospheres has proven to be an efficient way to remove metal nanoparticles from carbon nanotubes (CNTs). CNTs have a graphite structure, which has a thermal stability of up to 3000 °C, while metal particles evaporate at lower temperatures, especially in vacuum (VC) [1]. Thus, treatment at temperatures over 1800 °C yields multiwall carbon nanotubes (MWCNTs) with a high degree of purity [2]. However, the use of temperatures higher than 2000 °C for treatments of single-wall or doubled-wall CNTs may cause tube coalescence [3].

It is well known that even the best purification methods do not provide 100% purity, although in practice, an analysis of residual metal is seldom performed. Analyses of metal residue can identify metal phases and location of the residue sites. In addition, they may also be used to describe removal mechanisms. Knowledge of the impurities is extremely important for some applications of CNTs, mainly for biomaterials. Some tests in biological environments report that, depending on the media, metal particles encapsulated by carbon shells can be mobilized even for purified CNTs, which is called bioavailability [4–6].

This paper reports on a study of iron particles, a very common contaminant of MWCNTs produced with ferrocene [7]. It presents a detailed analysis of iron residues, in its solid phase, in MWCNTs purified by high temperature annealing in inert atmosphere (N_2) or under VC. Mössbauer spectroscopy (MS), X-ray diffraction (XRD) and X-ray Photoelectron Spectroscopy (XPS) allowed the monitoring of the residual iron in MWCNT samples. Moreover, the Raman spectra results show improvements in graphitic ordering after thermal annealing.

2. Methodology

The iron-containing phases in MWCNT samples are inherent to the production process. Samples produced by pyrolysis of camphor [8] mixed with 16% of ferrocene, at 850 °C in atmospheric pressure, provided the MWCNTs, as previously described elsewhere [9]. This is a very efficient production method, providing a mass yield around 30%, related to the pyrolysis of its initial mass.

Thermal annealing at high temperatures (1500–1800 °C) was performed with an ASTRO graphitic furnace by 2 h, in oxygen-free atmospheres, using N_2 (68.9 kPa) or VC (0.4 kPa), to remove the iron content from the MWCNTs. Thermogravimetric analyses (TGA) were used to determine the iron proportion in MWCNT samples after each treatment [10]. The TGA equipment was a Perkin Elmer, model 7HT, operating at temperatures ranging from 25 to 1100 °C at a heating rate of 10 °C/min in air.

* Corresponding author at: Instituto Nacional de Pesquisas Espaciais (INPE), Av. dos Astronautas, 1758, CEP 12.227-010, São José dos Campos, SP, Brazil. Tel.: +55 1232 086558; fax: +55 1232 086717.
E-mail addresses: ericafa@las.inpe.br, ericafa2009@hotmail.com (E.F. Antunes).

0169-4332 © 2011 Elsevier B.V. Open access under the Elsevier OA license.
doi:10.1016/j.apsusc.2011.04.090

Raman spectrums, recorded from 1000 to 3500 cm^{-1}, by using of a Renishaw 2000 system equipped with Ar laser (514.5 nm), showed improvement of the MWCNT crystalline structure after each treatment. The reduction in the relative intensity of bands and full width at half maximum (FWHM) [11] corroborate this improvement.

The MS was performed at room temperature with a ^{57}Co (Rh) source in constant acceleration mode used a triangular reference signal. The spectrums were computer analyzed in terms of model-independent distributions of hyperfine-parameter values.A study based on XPS evaluated the presence of iron and its oxidation state on MWCNT surfaces. The XPS analyzer was a commercial spectrometer (UNI-SPECS UHV), with a Mg K_α line ($h\nu$ = 1253.6 eV) and a pass energy set at 10 eV. The inelastic background of the C1s, O1s, and Fe2p electron core-level spectrums subtraction using Shirley's method prepared the spectrums for curve fitting. The calibration of binding energies was performed taking the hydrocarbon peak at 285.0 eV. Multiple Voigt profiles without constraints fitted the spectrums' features. The composition of the surface layer was determined from the ratio of the relative peak areas corrected by Scoffield sensitivity factors of the corresponding elements. The width at half maximum (FWHM) varied between 1.0 and 2.0 eV and the accuracy of the peak positions was ±0.1 eV.

A high resolution X-ray diffractometer (Philips X'Pert), equipped with a Cu K_α radiation tube, recorded XRD patterns in the 2θ scans ranging from 38° to 50° with grazing incidence angle of 3°.

An XL30 FEG scanning electron microscope (SEM), and a CM120 transmission electron microscope (TEM) from Philips enabled examining iron clusters and sites.

3. Results and discussion

The pyrolysis of camphor and ferrocene synthesized MWCNTs with diameters ranging from 15 to 50 nm and length of ~100 μm, with iron clusters inside the tubes and inside the structure of tube walls. Therefore, the contaminants to be extracted were essentially iron or iron carbide nanoparticles. Fig. 1 shows TEM images of as-grown MWCNTs and MWCNTs after thermal annealing at 1800 °C under VC by 2 h. In Fig. 1(a), for as-grown MWCNT, the dark points shown are iron nanoparticles in the nanotubes interior and inside their walls. However, Fig. 1b shows that, even at thermal annealing at 1800 °C under VC, a few iron particles remain inside nanotube walls.

SEM images reveal forming iron clusters on MWCNT surfaces during annealing at 1500 °C in N_2, as shown in Fig. 2a. However, the evaporation rate is higher under VC and no iron cluster can be seen in Fig. 2b and c, at 1500 °C and 1800 °C, respectively.

Fig. 3 shows TGA (a) and DTG (b) curves for the as-grown MWCNTs and annealed samples. The thermal stability of the MWCNTs in air improved considerably after annealing. As-grown MWCNTs showed oxidation peaks at a temperature of 615 °C, while treated samples showed peaks at 750 °C and 900 °C, after annealing at 1500 °C and 1800 °C, respectively. The residual mass for samples treated at 1800 °C under VC indicated 0.3% of total mass, which infers that is possible reaching a high degree of purity (higher than 99.7%). Notice that iron residue is an oxide, because of the presence of air during the TGA measurement; therefore, the iron content is actually lower than indicated.

Changes in thermal stability behavior can be correlated with improving the MWCNT crystalline quality after high temperature annealing. This improvement can be inferred from the noticeable narrowing in G band in Raman spectrum (Fig. 4) of samples treated at 1800 °C. The Raman spectrums of graphite-like materials present four main bands: D (~1352 cm^{-1}), G (~1582 cm^{-1}), D′ (~1600 cm^{-1}) and G′ (~2700 cm^{-1}), when analyzed by an Ar laser (514.5 nm). Generally, the ratio between the intensities of G and D bands (I_D/I_G) is used to evaluate the disorder degree of graphitic materials [12–17]. G′ band with high intensity is indicative of highly ordered nanographites, composed of few graphene sheets or 3D structures with defects on the lattice parameter because of curvature effect [18–20].

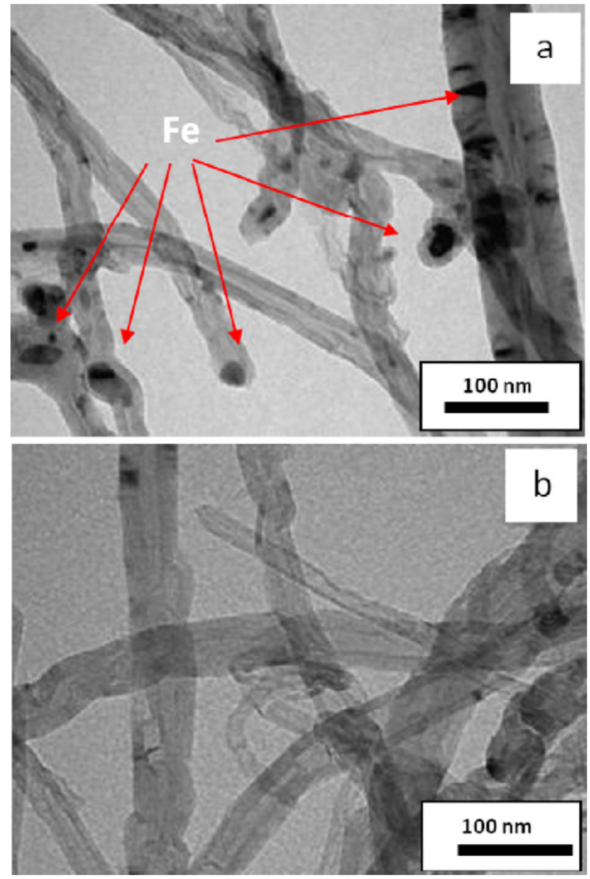

Fig. 1. TEM images of the iron located inside the nanotubes and into their walls: (a) as-grown MWCNT powder; (b) after purification at 1800 °C in VC.

Fig. 5 shows MS plots of the as-grown sample (a), and samples treated at: 1500 °C in N_2 (b), 1500 °C under VC (c), and 1800 °C under VC (d). Table 1 summarizes the relative spectral areas (RA) of all components, as determined by the adjustment of the spectrums. The analysis of the as-grown MWCNTs spectrum indicated the presence of Fe_3C (56%), α-Fe (16%), $Fe_{1-x}O_x$ (6%) and γ-Fe–C (22%), phases also observed by de Resende et al. [21]. Seventy eight percent of the iron phases detected in these samples have carbon in their structure (Fig. 5a). These phases are the result of MWCNT growth mechanisms, in which the metal particles are saturated by carbon until nanotubes nucleate [22,23]. During thermal annealing in N_2 at 1500 °C (Fig. 5b), the iron atoms in Fe_3C diffuse through nanotube walls. Consequently, the concentration of α-Fe is much higher (86%). In the treatment under VC at 1500 °C (Fig. 5c), most of the α-Fe evaporated, but is still responsible for

Table 1
Relative spectral areas got from adjusting the MS graphs of all samples.

Samples	Relative spectral area – RA (%)			
	Fe_3C	α-Fe	γ-Fe–C	$Fe_{1-x}O_x$
As-Grown MWCNT	56	16	22	6
N_2-1500 °C-2 h	–	86	9	5
VC-1500 °C-2 h	–	27	25	48
VC-1800 °C-2 h	–	–	32	68

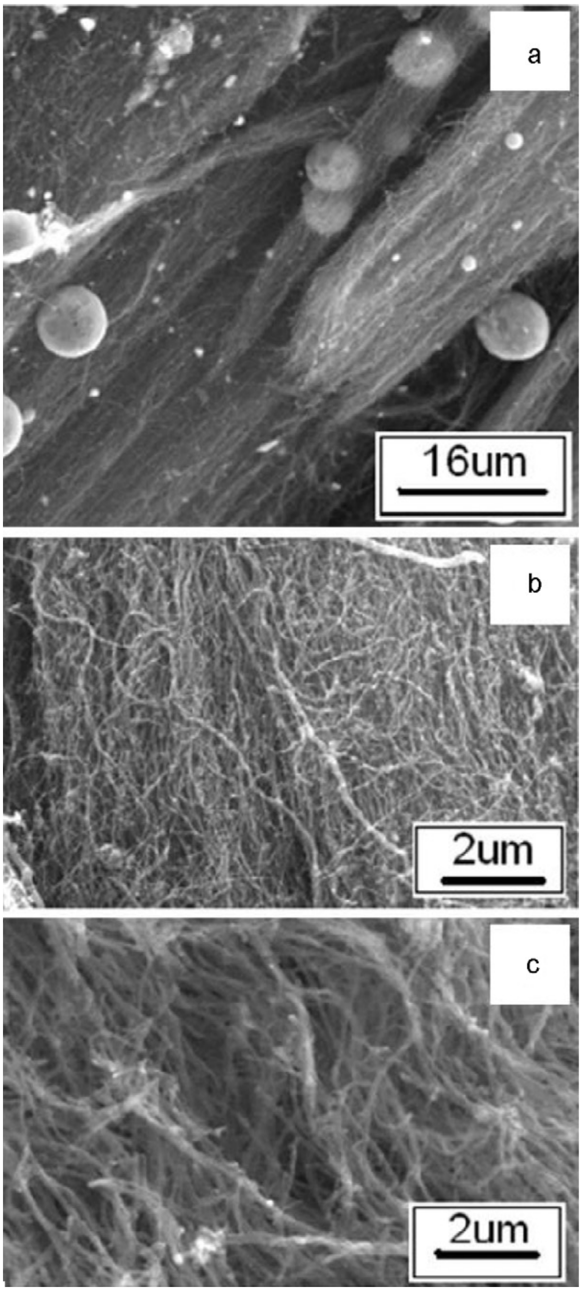

Fig. 2. SEM images of MWCNT powder after treatment at: (a) 1500 °C under N_2 atmosphere, (b) 1500 °C under VC, and (c) 1800 °C under VC.

27% of all iron phases. The α-Fe removal is completed at 1800 °C under VC (Fig. 5d). $Fe_{1-x}O_x$ was the most stable iron phase, and it was not eliminated even with thermal annealing at 1800 °C under VC. However, the signal got for this sample was rather lower compared to other samples (Fig. 5a–c), indicating that it has a very low iron content. This explanation is corroborated by its TGA curve, which showed a small amount of iron as residual mass (see Fig. 3).

Fig. 6 shows the MS graphs of a sample treated during 1 h duration at 1800 °C, carried out to check what occurs during the iron evaporation under VC. The fitting parameters showed one doublet due to wustite ($Fe_{1-x}O_x$) and three sextets with low values of hyperfine fields (8.7, 9.6, and 12.7 T). The three sextets suggest the presence of iron carbides [24,25]. The relative spectral area of the wustite was equal to 25%, whereas the three sextets due to the iron carbide phases composed 75% of the total spectrum.

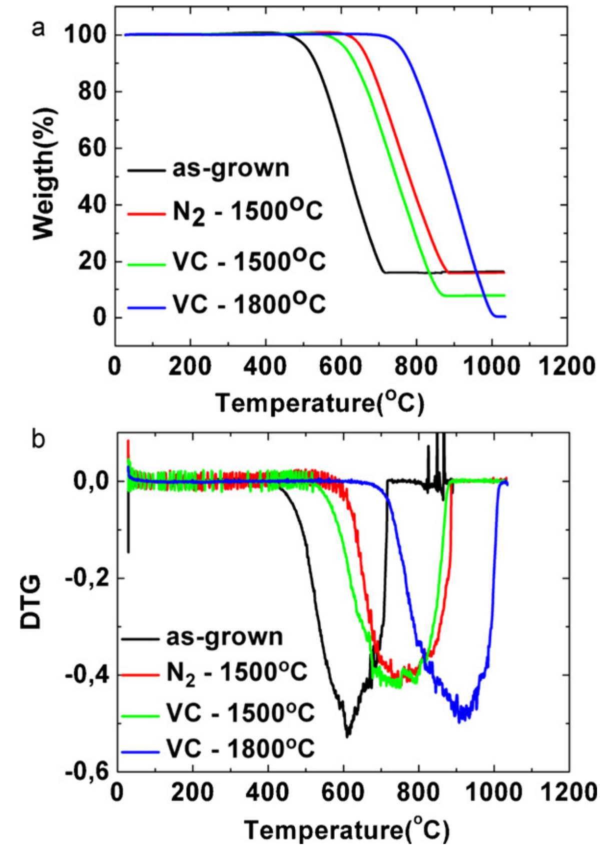

Fig. 3. Curves of TGA (a) and DTG (b) for the as-grown MWCNT powder, and samples treated by thermal annealing at 1500 °C and 1800 °C in N_2 atmosphere and under VC.

Fig. 7 shows the high resolution XRD pattern around the most intense iron diffraction peaks (38–50 °C), taken for all samples. The XRD diffractograms are in total accordance with MS graphs, showing diffraction peaks characteristic of Fe_3C, α-Fe, and γ-Fe–C [26–28]. Notice that the diffraction peak due to α-Fe phase is more intense for samples treated at 1500 °C in N_2, and it becomes weaker for samples treated under VC. The peak area of γ-Fe–C is higher than α-Fe after annealing under VC. The iron carbides also appear in the sample treated at 1800 °C under VC for 1 h. The sample annealed

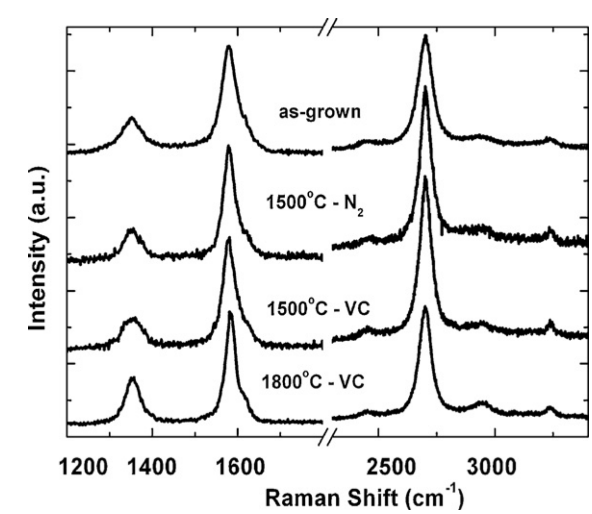

Fig. 4. Raman spectra at 514.5 nm for the as-grown MWCNT powder and samples treated by thermal annealing at 1500 °C and 1800 °C in N_2 atmosphere and under VC.

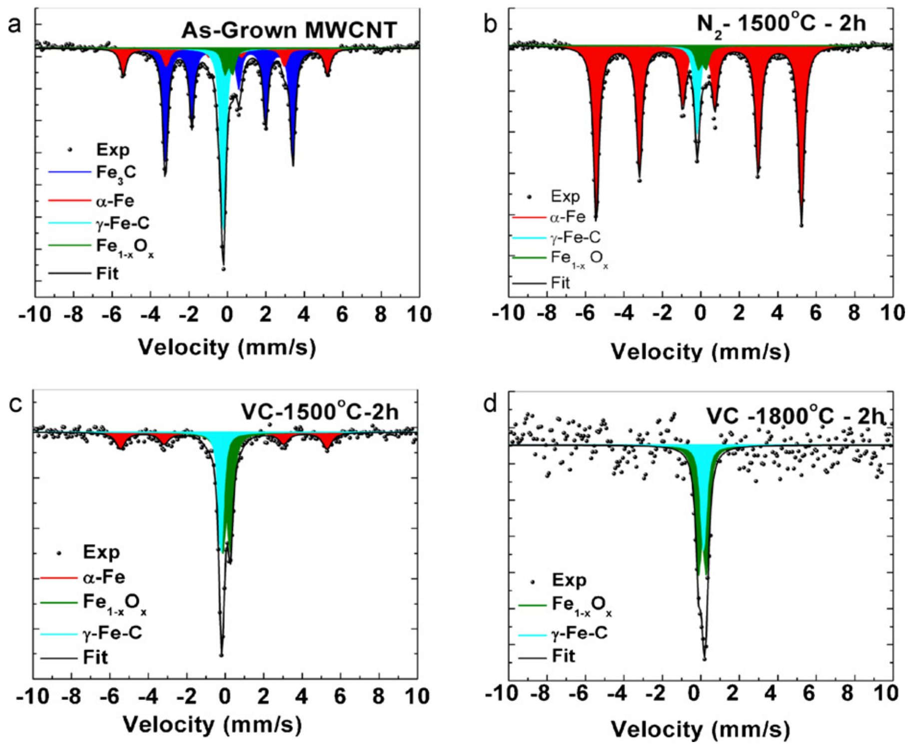

Fig. 5. MS graphs at room temperature for: (a) as-grown sample; and samples after treatment at (b) 1500 °C in N_2, (c) 1500 °C under VC, and (d) 1800 °C under VC. *Y*-axis is normalized and corresponds to transmission.

at 1800 °C under VC for 2 h, show the C(1 0 0) XRD peak of graphite almost totally free of iron.

Surface analyses carried out with XPS produced the plots shown in Figs. 8 and 9. Fig. 8 shows extended XPS graphs of: as-grown samples (a), and samples after treatment at: 1500 °C in N_2 atmosphere (b), 1500 °C under VC, (c), and 1800 °C under VC (d). They are very similar, showing 98.4 to 99.3% of carbon (∼284.5 eV), and the rest is oxygen (∼532 eV) and iron (710 eV) [29]. In fact, iron appeared only in the as-grown MWCNTs. In treated samples the iron content was below the detection limit (0.05 at%). Fig. 9 shows a comparison of high resolution C1s core level spectra for all samples in (a) and the deconvolution of Fe2p of the as-grown MWCNTs in (b).

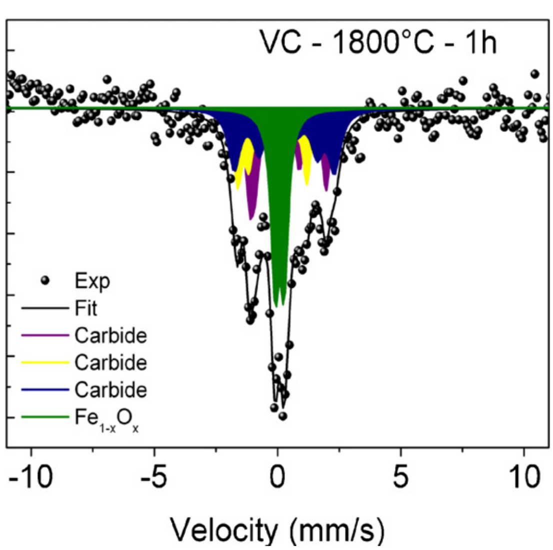

Fig. 6. MS graphs of the sample obtained from the treatment at 1800 °C during 1 h. The *y*-axis corresponds to transmission and it is normalized.

Notice that as-grown MWCNT spectrum in Fig. 9(a) is slightly broader than the purified ones. The C1s curve fitting was not presented here, but it usually is deconvoluted into six components: C–C (∼284.57 eV), C–H (∼285.19 eV), C–O (∼286.00 eV), C=O (∼287.38 eV), O–C=O (∼288.88 eV) and plasmon $\pi-\pi^{*}$(∼291.02 eV). When iron carbides are present, a component at ∼283.8 eV can be also included [30].

The iron spectrum (Fe $2p^{3/2}$) of the as-grown MWCNTs, measured at the detection limit, showed Fe^0 (707.0 eV) and minor contributions of iron oxides and carbides. The other peaks identified were: Fe_3C (708 eV), FeO_2 (709.8 eV), and Fe_2O_3 (711.0 eV) [31].

Fittings of O1s spectrums are shown in Fig. 9(c–f), for as-grown MWCNTs (c), and for samples treated by 2 h at: 1500 °C in N_2 (d), 1500 °C in VC (e), and at 1800 °C in VC (f). The O1 s

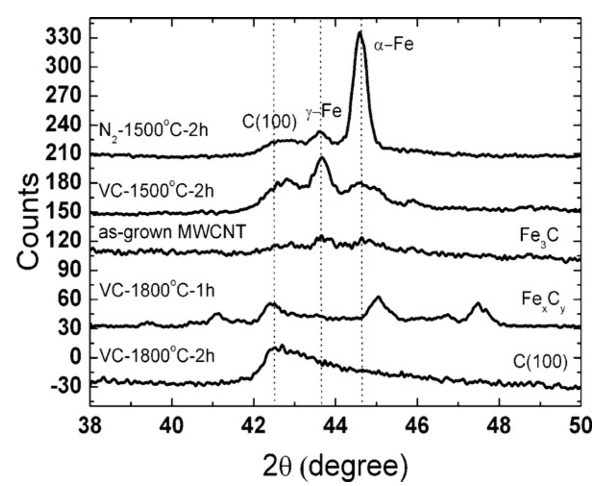

Fig. 7. XRD patterns for samples before and after thermal annealing.

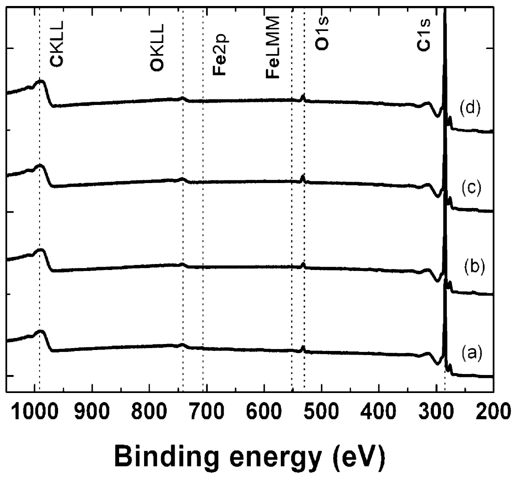

Fig. 8. Extended XPS graphs of: (a) as-grown sample; and samples after treatment at (b) 1500 °C in N_2 atmosphere, (c) 1500 °C under VC, and (d) 1800 °C under VC.

curves (Fig. 9 (c–f)) were fitted with three components, referent to C–O (∼533.3 eV), –OH/C=O (∼532 eV), and O^{-2} (∼530.2 eV) [32]. Although the iron spectrums (Fe 2p3/2) have not been identified on purified sample surfaces, the component referent to O^{-2} at the O1s core level is strongly indicative of iron presence in oxide forms. The O^{-2} component decreased with treatments at 1500 °C, but at 1800 °C under VC it vanished completely.

Basically, purification of CNTs consists in removing metal particles without degradation of the graphitic structure. In particular, for thermal annealing, the environment should be free of oxygen. In high temperature annealing, oxygen can react with carbon forming CO_2 or CO and graphitic walls are eroded. Hence both inert atmosphere and VC are appropriate for this treatment. The key in successful thermal annealing is that metal nanoparticles acquire mobility to diffuse through the graphitic structure without destroying C–C bounding. Graphite melts at temperatures around 3500 °C under an inert atmosphere, while iron melts at ∼1536 °C. The iron carbides formed during the MWCNT growth are clearly unstable during the annealing. Probably, over 1500 °C, the graphitic structure can dilate by increasing the vibration amplitude of carbon atoms of its hexagonal lattice. Meanwhile, iron nanoparticles are

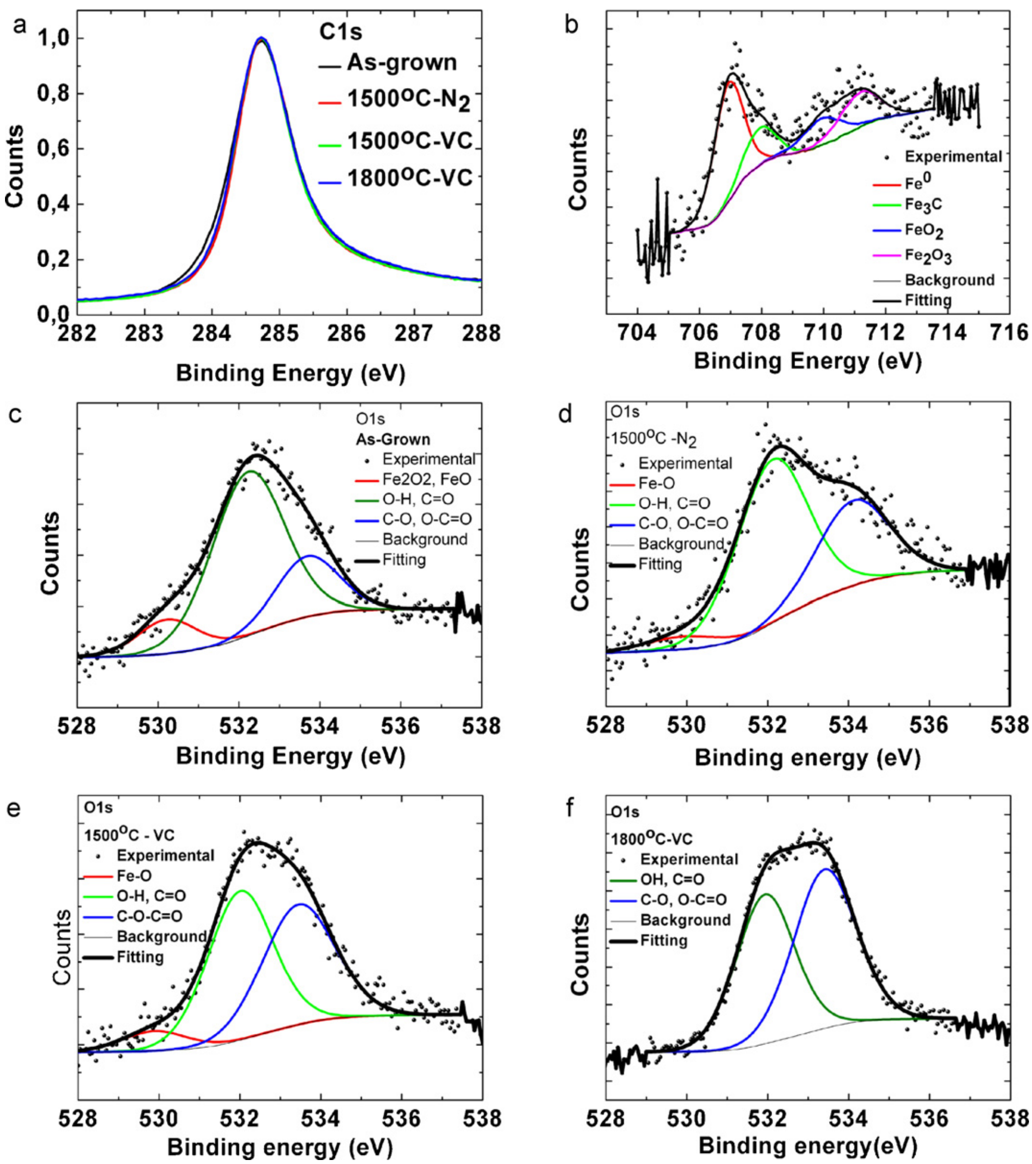

Fig. 9. XPS graphs of: (a) C1s core level of all samples, and (b) Fe2p core level of only as-grown MWCNT. Deconvolution of O1s core level for: (c) as-grown samples; and for samples treated at: (d) 1500 °C-N_2, (e) 1500 °C-VC, (f) 1800 °C-VC.

close to melting. Because of the higher spacing between C–C bounding [33–35] and the high mobility of iron in its liquid state the iron may diffuse to outside the tubes through their walls. The TEM images of Fig. 1b may indicate that diffusion occurred through the MWCNT walls. Outside the tubes, the iron may evaporate or diffuse onto MWCNT surface to form larger clusters. Higher temperatures lead to higher vapor pressures [36]. Under VC the evaporation rate is maximized because the pumping rate is higher than the evaporation rate. Under inert gas atmosphere the evaporation rate may decrease due to the increase of Fe partial pressure.

Treatments for only 2 h were insufficient to eliminate iron at 1500 °C in N_2, and spherical iron clusters can be found in some regions of CNT powder. These spheres most probably result from the iron diffusion with high mobility on the surface followed by condensation in larger clusters. From the near spherical form of these clusters, it can be inferred the contact angle between liquid iron and CNT surface is close to 180° under N_2 at the atmospheric pressure. That is, the MWCNT surface is super iron-phobic. This means that pure iron does not adhere to MWCNT, and their surface can be completely cleaned of iron residues.

Removal of iron oxide, on the other hand, needs complementary treatments in hydrogen environments or by acidic treatments in a liquid phase.

4. Conclusions

The high temperature thermal annealing successfully purified MWCNTs produced from camphor and ferrocene mixtures with ~15% of iron in their composition, achieving a purity degree higher than 99%. Heating under inert atmosphere or VC were essential to improve ordering of graphitic structures without significant carbon mass loss.

MS and XRD were effective in discriminating the sequence of iron removal, revealing key mechanisms of phase transformations. Even without specific treatment to open CNT tips, the iron atoms migrated from the nanotube core to the outside surface. Iron phases containing carbon (γ-Fe or Fe_3C) were removed more efficiently at higher temperatures and with VC pumping. XPS analyses also demonstrated very efficient iron removal from MWCNT surfaces.

These analyses have shown that only iron oxides remain stable after thermal annealing. Consequently, an increase in the degree of purity would only be achieved by oxide removal in longer treatments at higher temperature, or by a combination between higher temperature annealing and liquid-phase acidic treatments.

Acknowledgements

The authors acknowledge FAPESP for financial support, and Dr. Luis Cláudio Pardini (AMR/DCTA) for the use of the high temperature furnace.

References

[1] P.X. Hou, C. Liu, H.M. Cheng, Purification of carbon nanotubes, Carbon 46 (2008) 2003–2025.
[2] W. Huang, Y. Wang, G. Luo, F. Wei, 99.9% purity multi-walled carbon nanotubes by vacuum high-temperature annealing, Carbon 41 (2003) 2585–2590.
[3] Y.A. Kim, H. Muramatsu, T. Hayashi, M. Endo, M. Terrones, M.S. Dresselhaus, Thermal stability and structural changes of double-walled carbon nanotubes by heat treatment, Chem. Phys. Lett. 398 (2004) 87–92.
[4] X. Liu, V. Gurel, D. Morris, D. Murray, A. Zhitkovich, A.B. Kane, R.H. Hurt, Bioavailability of nickel in single-wall carbon nanotubes, Adv. Mater. 19 (2007) 2790–2796.
[5] X. Liu, L. Guo, D.G. Morris, A.B. Kane, R.H. Hurt, Targeted removal of bioavailable metal as a detoxification strategy for carbon nanotubes, Carbon 46 (2008) 489–500.
[6] A.O. Lobo, M.A.F. Corat, E.F. Antunes, M.B.S. Palma, C. Pacheco-Soares, E.E. Garcia e, E.J. Corat, An evaluation of cell proliferation and adhesion on vertically aligned multi-walled carbon nanotube films, Carbon 48 (2010) 245–254.
[7] C.N.R. Rao, R. Sen, B.C. Satishkumar, A. Govindaraj, Large aligned-nanotube bundles from ferrocene pyrolysis, Chem. Commun. (1998) 1525–1526.
[8] M. Kumar, Y. Ando, Chemical vapor deposition of carbon nanotubes – a review on growth mechanism and mass production, J. Nanosci. Nanotechnol. 10 (2010) 3739–3758.
[9] E.F. Antunes, E.C. Almeida, C.B.F. Rosa, L.I. de Medeiros, L.C. Pardini, M. Massi, E.J. Corat, Thermal annealing and electrochemical purification of multi-walled carbon nanotubes produced by camphor/ferrocene mixtures, J. Nanosci. Nanotechnol. 10 (2010) 1296–1303.
[10] D. Bom, R. Andrews, D. Jacques, J. Anthony, B. Chen, M.S. Meier, J.P. Selegue, Thermogravimetric analysis of the oxidation of multi-walled carbon nanotubes: evidence for the role of defect sites in carbon nanotube, Chem. Nano Lett. 2 (2002) 615–619.
[11] E.F. Antunes, A.O. Lobo, E.J. Corat, V.J. Trava-Airoldi, A.A. Martin, C. Veríssimo, Comparative study of first- and second-order Raman spectra of MWCNT at visible and infrared laser excitation, Carbon 44 (2006) 2202–2211.
[12] S. Lee, J.-W. Peng, C.-H. Liu, Raman study of carbon nanotube purification using atmospheric pressure plasma, Carbon 46 (2008) 2124–2132.
[13] M.S. Dresselhaus, G. Dresselhaus, R. Saito, A. Jorio, Raman spectroscopy of carbon nanotubes, Phys. Rep. 409 (2005) 47–99.
[14] A.C. Ferrari, J. Robertson, Interpretation of Raman spectra of disordered and amorphous carbon, Phys. Rev. B 61 (2000) 14095–14107.
[15] A.C. Ferrari, J. Robertson, Resonant Raman spectroscopy of disordered, amorphous, and diamond like carbon, Phys. Rev. B 64 (2001), 075414-1-075414-13.
[16] T.W. Ebbesen, T. Takada, Topological and SP3 defect structures in nanotubes, Carbon 33 (1995) 973–978.
[17] M.J. Matthews, M.A. Pimenta, G. Dresselhaus, M. Endo, Origin of dispersive effects of the Raman D band in carbon materials, Phys. Rev. B 59 (1999) R6585–R6588.
[18] E.F. Antunes, A.O. Lobo, E.J. Corat, V.J. Trava-Airoldi, Influence of diameter in the Raman spectra of aligned multi-walled carbon nanotubes, Carbon 45 (2007) 913–921.
[19] E.B. Barros, A.G. de Souza Filho, H. Son, M.S. Dresselhaus, G' band Raman lineshape analysis in graphitic foams, Vib. Spectrosc. 45 (2007) 122–127.
[20] A.C. Ferrari, J.C. Meyer, V. Scardaci, C. Casiraghi, M. Lazzeri, F. Mauri, S. Piscanec, D. Jiang, K.S. Novoselov, S. Roth, A.K. Geim, Raman spectrum of graphene and graphene layers, Phys. Rev. Lett. 97 (2006) 187401.
[21] V.G. de Resende, A. Peigney, E. de Grave, C. Laurent, *In situ* high-temperature Mössbauer spectroscopic study of carbon nanotube-Fe–Al_2O_3 nanocomposite powder, Thermochim. Acta 494 (2009) 86–93.
[22] T. Ruskov, S. Asenov, I. Spirov, C. Garcia, I. Mönch, A. Graff, R. Kozhuharova, A. Leonhardt, T. Mühl, M. Ritschel, C.M. Schneider, S. Groudeva-Zotova, Mössbauer transmission and back scattered conversion electron study of Fe nanowires encapsulated in multiwalled carbon nanotubes, J. Appl. Phys. 96 (2004) 7514–7518.
[23] P. Coquay, E. de Grave, R.E. Vandenberghe, A. Peigney, C. Laurent, Mössbauer spectroscopy involved in the study of the catalytic growth of carbon nanotubes, Hyperfine Interact. 139 (140) (2002) 289–296.
[24] O. Schneeweiss, R. Zboril, B. David, M. Hermánek, M. Mashlan, Solid-state synthesis of α-Fe and iron carbide nanoparticles by thermal treatment of amorphous Fe_2O_3, Hyperfine Interact. 189 (2009) 167–173.
[25] G. Le Caer, J.M. Dubols, M. Pijolat, V. Perrichon, P. Busslére, Characterization by Mossbauer spectroscopy of iron carbides formed by Fischer-Tropsch synthesis, J. Phys. Chem. 86 (1982) 4799–4808.
[26] R. Sergiienko, E. Shibata, Z. Akase, H. Suwa, T. Nakamura, D. Shindo, Carbon encapsulated iron carbide nanoparticles synthesized in ethanol by an electric plasma discharge in an ultrasonic cavitation field, Mater. Chem. Phys. 98 (2006) 34–38.
[27] N. Narkiewicz, W. Guskos, J. Arabczyk, T. Typek, W. Bodziony, G. Konicki, I. Gazsiorek, E.A. Kucharewicz, Anagnostakis, XRD, TEM and magnetic resonance studies of iron carbide nanoparticle agglomerates in a carbon matrix, Carbon 42 (2004) 1127–1132.
[28] E.D. Cabanillas, J. Desimoni, G. Punte, R.C. Mercader, Formation of carbides by electro-discharge machining of alpha iron, Mater. Sci. Eng. A276 (2000) 133–140.
[29] J. Kruusma, N. Mould, K. Jurkschat, A. Crossley, C.E. Banks, Single-walled carbon nanotubes contain residual iron oxide impurities which can dominate their electrochemical activity, Electrochem. Commun. 9 (2007) 2330–2333.
[30] F. Bonnet, F. Ropital, P. Lecour, D. Espinat, Y. Huiban, L. Gengembre, Y. Berthier, P. Marcus, Study of the oxide/carbide transition on iron surfaces during catalytic coke formation, Surf. Interface Anal. 34 (2002) 418–422.
[31] T. Fujii, F.M.F. de Groot, G.A. Sawatzky, F.C. Voogt, T. Hibma, K. Okada, *In situ* XPS analysis of various iron oxide films grown by NO_2-assisted molecular-beam epitaxy, Phys. Rev. B 59 (1999) 3195–3202.
[32] J.D. Walker, R. Tannenbaum, Characterization of the sol-gel formation of iron(III) oxide/hydroxide nanonetworks from weak base molecules, Chem. Mater. 18 (2006) 4793–4801.
[33] P.L. Walker Jr., H.A. Mckinstry, C.C. Wright, X-Ray diffraction studies of a graphitized carbon: changes in interlayer spacing and binding energy with temperature, Ind. Eng. Chem. 45 (8) (1953) 1711–1715.
[34] B.T. Kelly, The high temperature thermal expansion of graphite parallel to the hexagonal axis, Carbon 10 (1972) 435–438.
[35] H.O. Pierson, Handbook of Carbon, Graphite and fullerenes, Noyes Publications, New Jersey, USA, 1993.
[36] F.T. Ferguson, J.A. Nuth, N.M. Johnson, Thermogravimetric measurement of the vapor pressure of iron from 1573 K to 1973 K, J. Chem. Eng. Data 49 (2004) 497–501.